Single-atom Pt promotion of industrial Co-Mo-S catalysts for ultra-deep hydrodesulfurization

Christian Frederik Weise [a], Hanne Falsig [a], Poul Georg Moses [a], Stig Helveg [a,b], Michael Brorson [a], Lars Pilsgaard Hansen [a,*]

[a] Haldor Topsoe A/S, DK-2800 Kgs. Lyngby, Denmark
[b] Center for Visualizing Catalytic Processes (VISION), Department of Physics, Technical University of Denmark, DK-2800 Kgs. Lyngby, Denmark

A R T I C L E   I N F O

A B S T R A C T

We introduce a tertiary transition metal sulfide nanostructure, Pt-Co-Mo-S, for catalytic hydrodesulfurization (HDS) of sulfur-containing molecules in crude oil distillates with the aim to produce ultra-low sulfur transport fuels. The addition of ppm-levels of Pt to a standard industrial Co-Mo-S catalyst boosts the HDS activity by up to 46%. The promotional effect is examined by combining atomic-resolution Scanning Transmission Electron Microscopy (STEM), Energy Dispersive X-ray Spectroscopy (EDX), X-ray Absorption Near Edge Spectroscopy (XANES) and Density Functional Theory (DFT). It is shown that the Pt-Co-Mo-S catalyst contains predominantly single-layer MoS_2 nanocrystals with Co atoms fully covering the S-edge terminations and Pt atoms uniquely attached to corner and edge sites in a platinum(IV) sulfide-like structural motif. Platinum is suggested to reduce the sulfur binding energy and increase the abundance of coordinately undersaturated sites (CUS) and not necessarily changing the reactivity towards 4,6-DMDBT molecules, although more elaborate studies are needed to address this in detail.

1. Introduction

Since the 1970s societal focus on air quality and pollution control has introduced legislation requiring a continuous lowering of the sulfur content in transportation fuels implying that almost all crude oil (ca. 2500 million tons annually) is to be hydrotreated. In most of the world the maximum sulfur content in gasoline and diesel for road use is now 10 ppm, corresponding to a removal of 99.99% of the sulfur originally present. Hydrodesulfurization is the industrial catalytic process by which sulfur is removed from organosulfur molecules in mineral oil as H_2S at high hydrogen pressure and temperature (250–400 °C). The hydrodesulfurization process is sometimes more generally denoted hydrotreating as also organonitrogen compounds, aromatics and unsaturated carbon molecules in the oil undergo simultaneous conversion and/or are hydrogenated [1–3]. Over the last 40 years increasing severity of legislation has called for intense development of industrial hydrodesulfurization processes and catalysts. The main catalytic challenge for production of today's ultra-low sulfur diesel (<10 ppm sulfur) is the conversion of refractory alkyl-substituted dibenzothiophenes. These are molecules such as

4,6-dimethyldibenzothiophene (4,6-DMDBT) [4] that have alkyl substituents located in positions next to the sulfur atom and where the alkyl groups thus limit access to the sulfur atom.

Dr. Henrik Topsøe (1944–2019) [5] was a key figure in the research that established a detailed fundamental understanding of the nature of the industrially employed hydrodesulfurization catalyst, its active site(s), the molecular reaction routes and inhibition phenomena under ultra-deep hydrodesulfurization. Many of his groundbreaking and seminal contributions will be mentioned below including the discovery of the so-called Co-Mo-S structure that is now a commonly accepted model for the working hydrotreating catalyst. Characteristic to his work was a continuous employment of new and more sophisticated experimental methods and the combined use of results from multiple experimental and theoretical approaches, all with the aim to steadily uncover the secrets of hydrotreating catalysis. At Haldor Topsoe A/S, Henrik pursued the fundamental research in close interplay with industrial developments and fostered a synergy for implementation of the findings in industrial practice as visualized in Fig. 1.

In this paper, we will honor Henrik and his enormous impact on research and development in hydrotreating catalysis and acknowledge his unique generosity, mildness, humor, commitment and intellect, which made him a fantastic colleague and inspirational supervisor/mentor. The paper will present new findings for

---

* Corresponding author.
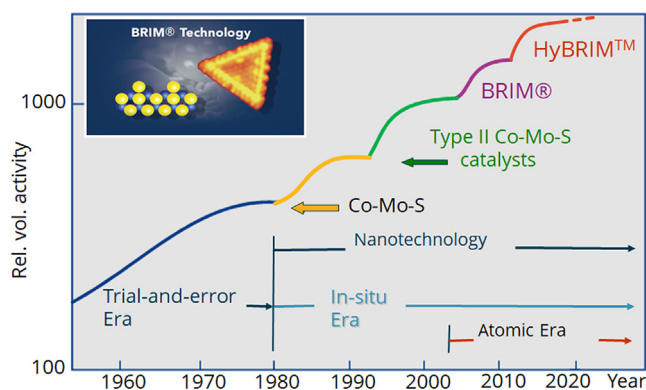   E-mail address: lpha@topsoe.com (L.P. Hansen).

Fig. 1. Development of industrial HDS catalysts. BRIM® and HyBRIM™ are Haldor Topsøe A/S proprietary catalyst technologies.

advancing hydrodesulfurization and thus lie at the heart of Henrik's interests. Although Henrik was not part of the present work, it testifies that the tradition of research and methodologies that he established in the laboratories of Haldor Topsoe A/S are deeply embedded and form the basis for continuous developments of even rather mature catalytic systems.

1.1. Molybdenum-based hydrodesulfurization catalysts and the Co-Mo-S model

Sweetening of gasoline was in the first part of the 1900s undertaken by non-catalytic processes involving absorption or conversion of the odor-repulsive mercaptans by means of agents such as metallic copper or lead sulfide. Subsequently conversion of organosulfur compounds was claimed using molybdenum-sulfur or tungsten-sulfur materials as catalysts, but actual catalysis was not documented before 1943 when it was discovered that the bimetallic combination cobalt-molybdenum had an extraordinary ability for catalytic hydrodesulfurization [6]. In the context of hydrotreating, cobalt is traditionally termed a promoter (to molybdenum) but as the boost in activity is a factor of 10–20 this terminology is somewhat misleading. The 1943 paper also examined the combinations iron-molybdenum, copper-molybdenum, zinc-molybdenum and aluminum-molybdenum to find that they had much inferior catalytic performance. Soon it was found that the combination nickel-molybdenum also had high catalytic activity and this combination is together with cobalt-molybdenum universally employed in industrial hydrotreating today. The chemical state of the catalytically active metals at process conditions was known to be at least partially sulfidic and in some early models sulfidic Mo was bonded via oxygen to the surface of the high-surface area alumina support employed. It was eventually realized that Mo was in a chemical state like MoS_2, i.e., with no or very limited amounts of bonds to alumina surface. The precise role of the promoter element cobalt (also itself in a sulfidic state) was yet unresolved. Two models were considered [1]. The first, a contact synergy model in which separate Co_9S_8 and MoS_2 nanostructures together were responsible for the hydrotreating catalysis with a spill-over of activated hydrogen. The second, an intercalation model in which the promoting Co atoms were located in the van der Waals gap between the layers of the layered MoS_2 structure, similarly to how layered MoS_2 structures may intercalate e.g., lithium ions. In 1976 a team led by Henrik Topsøe found by *in situ* Mössbauer Emission Spectroscopy (MES) that cobalt in sulfidic cobalt-molybdenum catalysts occurred in 3 different forms [7]: (i) Co_9S_8, (ii) $CoAl_2O_4$ and (iii) a new form distinctly different from the two-former mentioned. Both Co_9S_8 and $CoAl_2O_4$ may sometimes be present in catalysts but neither of the compounds

contribute in any significant extent to the catalytic activity [8–10]. On the other hand, a clear correlation between the size of the MES cobalt signal and the catalytic activity within a series of cobalt-molybdenum catalysts made it possible to assign the catalytically active center to what was named the Co-Mo-S structure [8,9]. It was in 1981 found by Extended X-ray Absorption Fine Structure (EXAFS) [11] that Mo was present as MoS_2-like nanodomains and the so-called Co-Mo-S model was proposed which has Co atoms located on the edges of the layered MoS_2 structure. A high affinity of Co for the edges of MoS_2 has since been confirmed by Scanning Tunneling Microscopy (STM) [12] of Co-Mo-S structures synthesized on Au(1 1 1) and by Scanning Transmission Electron Microscopy (STEM) [13] of carbon supported Co-Mo-S synthesized by metals impregnation and subsequent gas phase sulfidation. In parallel with the technical progress in atomic resolution imaging, Density Functional Theory (DFT) methods evolved and have now been able to elucidate the catalytic mechanisms taking place at active sites located on the edges of Co-Mo-S nanocrystals [14–18].

Generally, two hydrodesulfurization pathways are in play for HDS of dibenzothiophenes, the direct desulfurization (DDS) and the pre-hydrogenation (HYD) pathways [19]. By the DDS pathway, direct cleavage of the C—S bond(s) in the dibenzothiophene molecule takes place and with a minimum amount of H_2 consumed. By the HYD pathway, the dibenzothiophene molecule undergoes an initial hydrogenation in one of its six-rings followed by cleavage of C—S bond(s). In this way the HYD pathway consumes more H_2 than the DDS pathway. Whereas molecules such as thiophene and dibenzothiophene are primarily hydrodesulfurized by a DDS pathway then HDS of sterically hindered dibenzothiophenes, such as 4,6-DMDBT, proceeds mainly via a HYD pathway in the model feed studies required to detect and quantify the individual desulfurized product molecules [20–22]. The detailed reaction mechanisms are still debated. Following the DDS pathway, the current view of the catalytic cycle is that sulfur vacancies are created on cobalt atoms (associated with $\bar{1}$0 0 S-terminated edges of MoS_2) by formation of H_2S by means of atomic hydrogen formed by activation of H_2 at the metallic so-called brim sites at the edge of the MoS_2 structure [23–25]. The sulfur atom of an organosulfur molecule attaches to a cobalt atom at a coordinative undersaturated site (CUS) such as a sulfur vacancy and after transferal of more activated hydrogen atoms generated at the nearby brim sites the carbon part of the organosulfur molecule dissociates into a main hydrocarbon part and a single sulfur atom. Molecular hydrodesulfurization has now taken place and subsequently sulfur atom removal as H_2S by means of yet more activated hydrogen from the brim sites takes place to close the cycle. STM imaging have revealed organosulfur molecules associated with edge sites for sufficiently long time to capture an STM image, thus providing unprecedented insights and direct visualization of the important first adsorption step in the catalytic process [26–28].

1.2. Promotion of MoS_2 by other metals than Co and Ni and by more than one metal

Experimental microscopy techniques and DFT calculations give, for Co and Ni promoted MoS_2, a mutually consistent image of the nature of the active sites on the MoS_2 edges. No other first transition period metals have experimentally to the same substantial degree been found to promote the hydrodesulfurization reaction. For instance, an STM-based study [29] has shown that all four metals Co, Ni, Cu and Zn associate to MoS_2 edges in identical ways, i.e., association to the edge is a necessary but not sufficient prerequisite for promoting the catalysis. As Cu and Zn do not have any promoting effect [29], the electronic structure of the potentially

promoting element clearly plays a role and only for Co and Ni do the electronic structure seem suited for hydrodesulfurization catalysis. DFT calculations have shown that when Fe is placed on an MoS_2 edge in the very same way as Co, then the Fe-Mo-S system is characterized by sulfur binding parameters that suggests low catalytic activity [30]. Going to the second and third transitions periods, Rh-Mo and Ir-Mo catalysts have experimentally [31–37] shown substantially higher activities than a Mo-only catalyst, i.e., the two elements Rh and Ir promote to a comparable extend to their first transition period counterpart Co. Oppositely, the element combinations Ru-Mo, Pd-Mo and Pt-Mo did not provide catalysts with a substantially enhanced HDS activity compared to a Mo-only reference [37–40]. All in all, only Co, Ni, Rh and Ir have been found to substantially promote MoS_2.

In industrial practice, a particular hydrotreating reactor is designed with a certain size and maximum pressure. To get the best performance, the refiner will choose a catalyst by considering both the specific oil feed (nature of crude, boiling point range) and the achievable hydrogen amount and pressure. In this context Co-Mo is typically the preferred catalyst for relatively low hydrogen partial pressures (<40 bar) whereas Ni-Mo is preferred for high pressure (>60 bar) applications. This has, over the years, led to many catalyst producing companies launching all-in-one catalysts that contain both Co and Ni as promoting elements. Although such element combinations may indeed at certain operating conditions give moderate advantages in terms of catalyst performance, it is certainly not the case that the combination provides the refiner with the very best of *both* Co and Ni. Rather, these Co-Ni-Mo catalysts have performance characteristics that are probably closer to a kind of average of the Co and Ni catalyst performances, i.e., the performance you would get from loading a physical mixture of Co-Mo and Ni-Mo catalysts. Bimetallic promotion of MoS_2 with Ni-Cu has also been examined but with no great industrial breakthrough [41].

The complexity of the hydrodesulfurization reaction mechanisms as well as the structural complexity of the bimetallic transition metal sulfide nanostructures have hampered a detailed understanding of all empirical findings of promotional effects. However, with the toolbox at hand today and with the multidisciplinary approach that Henrik was so dedicated to, we will in this paper explore a metal combination Co-Pt that has had very limited attention [42]. Specifically, we will demonstrate how, in our hands, highly activity-enhanced Pt-Co-Mo-S nanocrystals can be prepared by slight modifications of the otherwise standard Co-Mo-S catalyst and we will present an atomistic picture for the synergetic role of this tertiary transition metal sulfide catalyst system.

2. Experimental

2.1. Catalyst preparation

Pt-containing Co-Mo catalysts were prepared in two different ways: (i) by post impregnation of Pt onto a commercial (unsulfided) Co-Mo/Al_2O_3 catalyst (16 wt% Mo and 3.5 wt% Co) and (ii) to illustrate the feasibility of a more industrially acceptable preparation route, by incipient wetness impregnation of alumina carrier extrudates with a Co-Mo liquor into which Pt had been incorporated. For the former preparation method [Pt(acac)$_2$] (acac = acetylacetonate), corresponding to the desired wt% of Pt on the final catalyst, was dissolved in a volume of dichloromethane (DCM) corresponding to the pore volume, as determined by mercury porosimetry, of the oxidic Co-Mo catalyst to be modified. After 30 min impregnation time, the sample was air dried at room temperature for 30 min followed by drying at 250 °C in air for 1 h. For the latter preparation method, [Pt(NH$_3$)$_4$](HCO$_3$)$_2$ was dissolved

into a commercial Co-Mo liquor, followed by pore volume filling impregnation of an alumina carrier. This also yielded catalysts with 16 wt% Mo and 3.5 wt% Co. After preparation the catalysts obtained by one or the other method differed neither in chemical properties nor activity within the uncertainty of the activity measurements. Samples with a specific nominal loading of Pt are in the following referred to as Pt-Co-Mo(wt%).

2.2. Catalytic testing

The catalyst samples were tested in a 5-in-1 pilot unit in which 5 reactors are placed closely together thus experiencing the same thermal conditions. The reactors were loaded with a mixture of 15.0 mL neat catalyst volume (whole extrudates) and 40% fine inert SiC particles. In one 5-in-1 test 4 platinum-modified experimental catalysts were tested together with the commercial reference sample that was used as basis for the platinum impregnations. After loading of the reactors, the catalysts were sulfided for 24 h at test condition using a sulfur doped oil. After the sulfidation procedure a switch to the test feed was made and the pilot unit was then run for 110 h at steady conditions. Samples were collected simultaneously from all 5 reactors at run hours 80, 90, 100 and 110. The activities reported are based on the average sulfur level of the 4 samples collected. Sulfur-content variation between the 4 samples obtained at different run hours was minimal. The activities have been calculated using our internal kinetic model to obtain relative rate constants with the industrial reference catalyst used for the impregnation experiments defining activity of 100%. Test conditions: 355 °C, 30 barg H_2, 1.5 LHSV, 490 H_2/oil, 75/25 w/w blend of straight run diesel (LG) and cracked feed (LC). Feed properties: 1.22 wt% S, 356 wtppm N, SG 60/60 0.8735, calc. D86: 237 °C (10 vol%), 297 °C (50 vol%), 358 °C (90 vol%). The tested Pt-Co-Mo catalysts were collected from the reactor after cooling to RT. Then the samples were sieved and rinsed several times with an excess of pentane to wash away oil residues inside and outside the porous extrudates. All volatiles were removed by drying the sample at 40 °C in vacuum and the samples were subsequently stored in closed containers until characterization by electron microscopy or X-ray absorption was undertaken.

2.3. Electron microscopy

Electron microscopy examinations were performed using an FEI Talos F200X (scanning) transmission electron microscope equipped with ultra-bright field emission gun (X-FEG) and Super-X EDX detectors. The microscope was operated at 200 keV in both scanning-beam and broad-beam modes. In the scanning-mode, a high-angle annular dark field (HAADF) detector was employed for imaging concurrently with EDX spectrum acquisition. In the broad-beam mode, a charge-coupled device camera was used for imaging. The combined HAADF and EDX data cube was acquired for 30 min over an area of 1024 pixels × 1024 pixels (0.26 nm pxl^{-1}) with a probe current of 0.7 nA and EDX energy range of 0–20 keV (0.01 keV/channel). Samples for electron microscopy were prepared by crushing the catalyst pellets in a mortar and dispersing the fine powder onto a Cu-TEM grid with continuous carbon (SPI Supplies) in ambient conditions. Thus, the samples have been exposed to ambient conditions for a few days during transportation and storage before examination in the electron microscope.

To increase the counting statistics of a single EDX pixel spectrum the data were binned by a factor of x8 to yield an effective pixel size of 2.1 nm and further processed in Brüker software (Esprit 1.9) by a Bremsstrahlung background subtraction, series deconvolution and Cliff-Lorimer quantification to display the net counts. The Pt-Lα (9.435 keV) signal, however, showed too few

Christian Frederik Weise, H. Falsig, Poul Georg Moses et al.

Journal of Catalysis 403 (2021) 74–86

counts for a proper background subtraction and therefore are displayed as raw counts with an estimated signal-to-noise of 50% as determined from the peak-to-background in the summed EDX spectrum. The Pt-L region was emphasized because it separates from other elemental peaks, in contrast with e.g. the Pt-M_α signal (2.050 keV) that overlaps with Zr L_α (2.044 keV) signals as reminiscence from the microscope. Likewise, the present analysis focuses on Mo-K_α (17.480 keV), Co-K_α (6.931 keV) and S-K_β (2.465 keV) that all separates peaks stemming from the sample and microscope.

High-resolution scanning transmission electron microscopy (HRSTEM) was performed on a JEOL ARM-200F equipped with cold field emission gun (CFEG) and CEOS probe (STEM)-Cs-corrector. The microscope was operated at 200 keV and probe aberrations up to 3rd order was corrected. The illumination system was set with a probe size of ~ 1 Å, with a current of approximately 0.1 nA, and with a pixel dwell-time of 32 μs. The focusing of the sample was done prior to acquisition in an adjacent area as to record an image of a pristine area not previously exposed to the electron beam. Images were generated using a high-annular dark-field detector. Although residual oil is removed by pentane as described in section 2.2, HRSTEM revealed carbon deposition to a degree that varied from area to area. Occasionally areas allowed sufficient cleanliness to acquire an HRSTEM image of a clearly atom-resolved image and the atomic details blurred after a few scans, so it was necessary to move to a new area. It was such images that have been considered in the present study. Even though further optimization of beam energy and current could be pursued, Fig. S8 (Supplementary Material) indicates that some Pt atoms are stabilized in successive images suggesting they reveal their pristine locations. Complementary STEM image simulations were carried out in the QSTEM software suite with experimental details shown in Supplementary Material.

2.4. X-ray absorption spectroscopy

The activity tested Pt-Co-Mo(0.5) catalyst was, in its sulfided state as retrieved from the reactor, characterized *ex situ* by X-ray absorption near edge structure (XANES) at the XAS beamline at the ANKA synchrotron source (Karlsruhe, Germany) using the Pt L_3-edge (11.564 keV). The catalyst was crushed and pressed into a 13 mm pellet using polyethylene and measured in transmission mode. The XANES spectra were energy calibrated using a metal reference, background subtracted and normalized. References of PtS (ICSD_31131) and PtS$_2$ (ICSD_41375) were also measured.

2.5. Density functional theory (DFT)

To obtain total energies we employed the GPAW [43,44] density functional theory code in the finite difference mode with a spacing of 0.18 Å. The exchange and correlation were treated using the BEEF-vdW functional [45]. As in ref. [25], the S-edge and Mo-edge of the Co-Mo-S particle were modelled with 4x4 stripes periodic in the x-direction and separated with vacuum in the y and z directions. The corner of the Co-Mo-S particle was modeled with a step stripped continuous in the x-direction separated by vacuum in the y and z directions, exposing 3xCo and 2xMo on the S- and Mo-edge respectively. A 2x1x1 Brillouin zone sampling was used in the x, y and z direction respectively. All structures were optimized until the maximum force was lower than 0.03 eV/Å. The crystal structures of PtS$_2$, MoS$_2$ and Co$_8$S$_9$ were optimized using the stress tensor method available in ASE [46]. In the following, the free energy of gas phase H$_2$ and H$_2$S has been obtained using the ideal gas approximation [47]

$$G_x = E_x + ZPE_x + \Delta H_x^{0,T} - TS_x^T + k_B T \ln\left(\frac{p_x}{p}\right)$$

where E_x is the electronic energy, ZPE_x the zero-point energy, $\Delta H_x^{0,T}$ the change in enthalpy from 0 K to T, S_x^T the entropy at T, p_x the pressure of the molecule in the gas, and p the standard pressure, and the free energy of surfaces and bulk sulfides are assumed to be described by the 0 K electronic energy. The uncertainty of the calculation has been estimated using the BEEF-vdW ensemble [45], using an ensemble of 3000 energies. This uncertainty represents how much, e.g., an adsorption energy (at 0 K) can vary within the GGA functionals.

We obtain the sulfur equilibrium termination at HDS conditions, 673 K and p(H$_2$)/p(H$_2$S) = 20, for the S-edge, Mo-edge and at the corner by gradually increasing the sulfur coverage and for each step calculating free energy change of the sulfidation according to:

$$\text{Co}_x\text{Mo}_y\text{S}_{z-1} + \text{H}_2\text{S(g)} \leftrightarrow \text{Co}_x\text{Mo}_y\text{S}_z + \text{H}_2\text{(g)} \qquad (1)$$
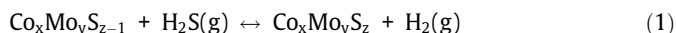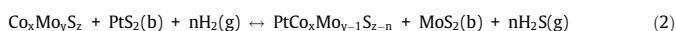
where x, y and z represent the number of Co, Mo and S atoms in the supercell, respectively.

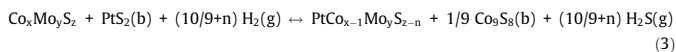The adsorption energy of a molecule on a specific site, ΔE_x, has been obtained as follows:

$$\Delta E_x = E_{x*} - E_x - E_*$$

where E_{x*} is the energy of the adsorbed molecule on a specific site, E_x the energy of the molecule in vacuum, and E_* the energy of the site.

The stability of single atom Pt incorporation at the Mo-edge is described by the free energy of the following reaction:

$$\text{Co}_x\text{Mo}_y\text{S}_z + \text{PtS}_2(\text{b}) + n\text{H}_2(\text{g}) \leftrightarrow \text{PtCo}_x\text{Mo}_{y-1}\text{S}_{z-n} + \text{MoS}_2(\text{b}) + n\text{H}_2\text{S(g)} \qquad (2)$$

where Co$_x$Mo$_y$S$_z$ here represents the equilibrium structure of the Mo-edge, PtCo$_x$Mo$_{y-1}$S$_z$ is the equilibrium structure of the Pt doped Mo-edge, where 1 Mo at the edge has been substituted with 1Pt in the unit cell, and PtS$_2$ and MoS$_2$ are the reference metal sulfides of Pt and Mo, respectively. Similarly, at the Co-promoted S-edge and corner site, the stability of Pt is described by calculating the free energy change of the reaction:

$$\text{Co}_x\text{Mo}_y\text{S}_z + \text{PtS}_2(\text{b}) + (10/9+n)\,\text{H}_2(\text{g}) \leftrightarrow \text{PtCo}_{x-1}\text{Mo}_y\text{S}_{z-n} + 1/9\,\text{Co}_9\text{S}_8(\text{b}) + (10/9+n)\,\text{H}_2\text{S(g)}$$
$$(3)$$

where Co$_x$Mo$_y$S$_z$ here represents the equilibrium structure of the S-edge/corner of a Co-Mo-S particle, PtCo$_{x-1}$Mo$_y$S$_z$ the equilibrium structure of the Pt doped S-edge/corner site, and PtS$_2$ and Co$_9$S$_8$ the stable metal sulfides of Pt and Co respectively.

3. Results and discussion

3.1. HDS activity

The hydrodesulfurization (HDS) activity of the Pt-Co-Mo catalysts was measured relative to a commercial Co-Mo reference catalyst under industrially relevant conditions in a pilot unit. The activities are reported as relative volume activities. All (Pt)-Co-Mo catalysts measured have, within the experimental uncertainty of preparation using the same alumina carrier and the experimental uncertainty of subsequent chemical analysis, identical molar loads of molybdenum per volume (and weight) of catalyst. Fig. 2a shows the influence of increased amounts of platinum in the catalysts. The activity increases approximately linearly up to about 1 wt% Pt (10000 ppm) and here reaches an unparalleled catalytic performance of 146%. Platinum in amounts higher than 1 wt% did not increase activity further and eventually a slight

Christian Frederik Weise, H. Falsig, Poul Georg Moses et al.

Journal of Catalysis 403 (2021) 74–86
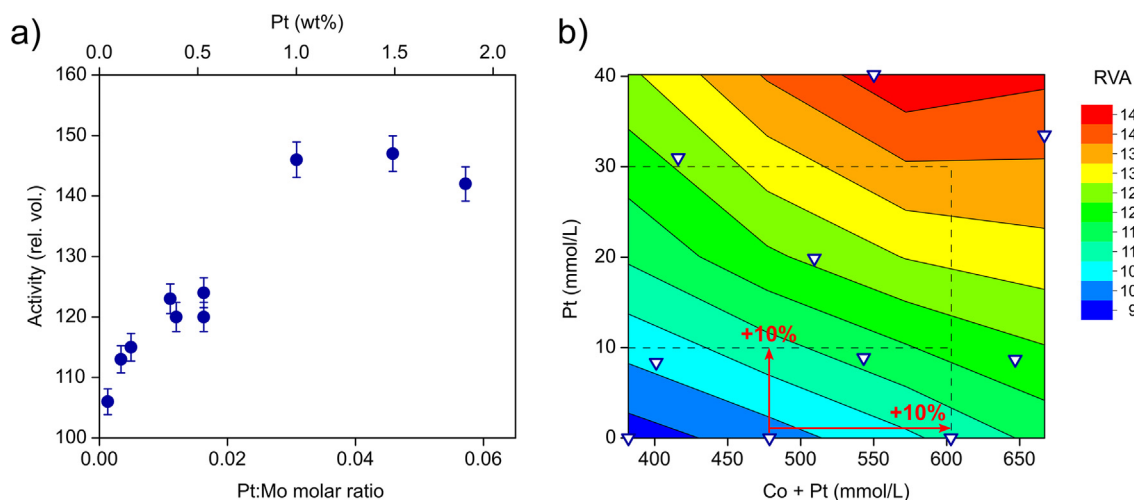
Fig. 2. (a) HDS activity of Pt-Co-Mo catalysts with increasing Pt content while keeping Co and Mo content in the reactors fixed. Error bars represent typical uncertainties of ± 2% in the activity measurements. (b) Contour plot of HDS relative volume activity (RVA) as function of Pt and total promoter (Co + Pt) concentrations in 10 reactor tests of catalysts with varying amounts of Co and Pt with a fixed Mo content. Equidistant contour lines correspond to a linear trend. Dashed lines are guides-to-the-eye.

decrease in activity was found. This may suggest a saturation and a corresponding Pt waste of the promotional active sites at high platinum loadings. The activity of catalysts without any cobalt at all, Mo/Al$_2$O$_3$ and Pt-Mo/Al$_2$O$_3$, was found to be at least an order of magnitude lower than that of the Co-Mo reference catalyst of Fig. 2a. Thus, it must be the intimate contact of Co and Pt that is responsible for the boosted performance.
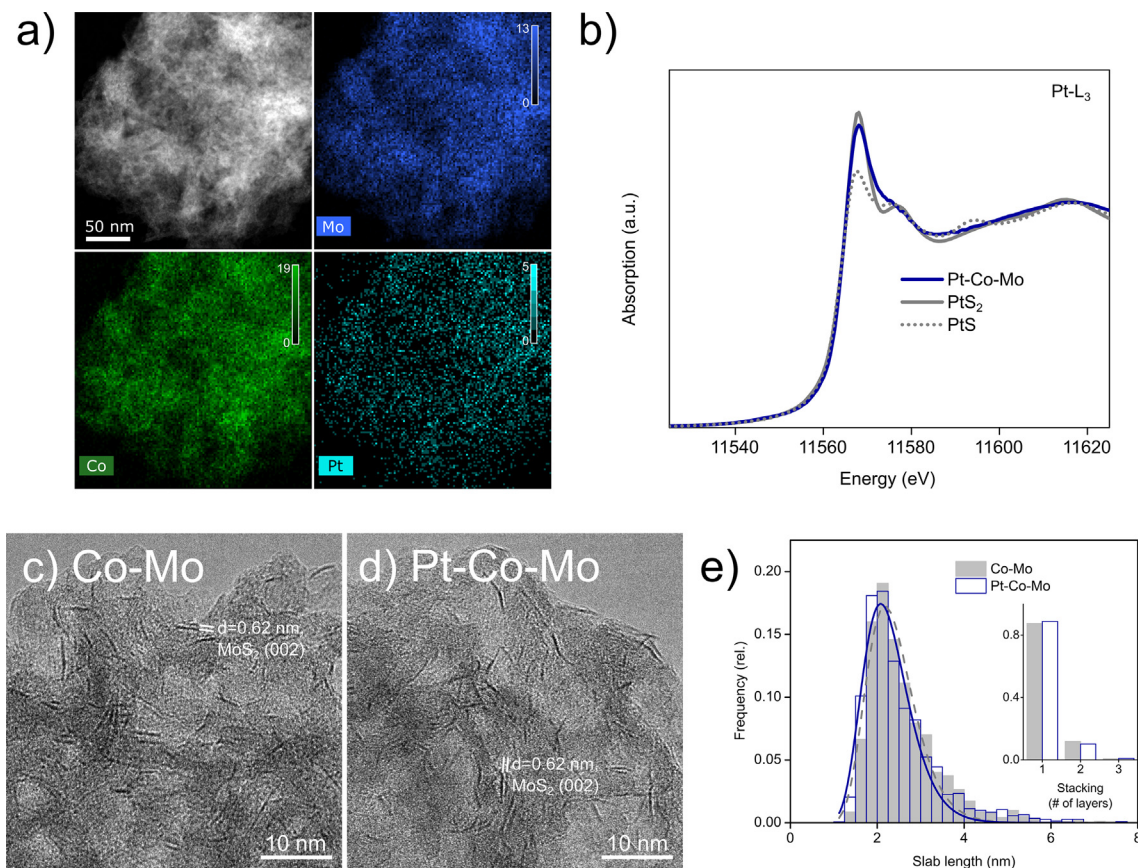
Fig. 2a shows a Pt promoted activity for a fixed cobalt amount. Samples with variations in Co amounts were prepared as well. Fig. 2b shows the effect of variations in the amount of both promoters (Pt and Co) while keeping the molar Mo amount constant. The contents of Pt and Co are shown as estimated volumetric concentrations (mmol/L) inside the reactor during catalytic testing. In Fig. 2b, the activity increases with an increased amount of Co (following the x-axis, y = 0). An increase in activity of 10% was obtained by an increase in the Co concentration from 479 mmol/L to 603 mmol/L in the reactor, corresponding to 124 mmol/L or 26% of the total Co in the reference sample. The Pt effect is much more pronounced: a similar activity increase of 10% is obtained by replacing only 10 mmol/L of Co (~2% of total Co) with Pt (following the y-axis). Thereby, in the concentration domains examined, the intrinsic promotional effect of platinum (per atom) is more than 12 times higher than cobalt in a rather large window of promotor concentration variations of the industrial Co-Mo catalyst. Because of the very consistent data, navigating in the activity contour plot by simple extrapolation now allows for tailoring the catalyst activity with the usage of cobalt and platinum in combination. For instance, at a fixed low Pt amount of 10 mmol/L, an activity lift of 20% RVA can readily be obtained, and likewise for 30 mmol/L of Pt an activity boost of more than 35% is expected as indicated by dashed lines in Fig. 2b.

3.2. Characterization of Pt-Co-Mo catalysts

Selected Pt-Co-Mo catalysts were after catalytic HDS activity tests characterized by electron microscopy and X-ray absorption spectroscopy in order to unravel the nature of the Pt-promotion. Fig. 3a shows a STEM image of the activity tested Pt-Co-Mo(0.5) catalyst with the corresponding EDX element maps displaying the distribution of cobalt, molybdenum and platinum. The metals are all uniformly distributed on the agglomerate together with EDX signals of sulfur, aluminum and oxygen in accordance with an alumina-supported (sulfided) Co-Mo catalyst (Fig. S3, Supple-

mentary Material). The elemental composition of various sample agglomerates observed in the STEM imaging appeared surprisingly homogeneous (based on at least 20 agglomerates for the Pt-Co-Mo (0.5) sample) and despite a very little platinum detection signal in a single pixel spectrum (see Fig. S4, Supplementary Material) a Pt peak signal was verified throughout the catalyst from larger EDX sum-spectra areas. In fact, a quantification of the Pt amount from the full area EDX sum spectrum, as well as a selected smaller area, revealed a similar Pt content of 0.5 wt% demonstrating a high homogeneity within the sampled area, and indicates a uniformity on a larger scale as it matches the nominal platinum load in the prepared catalyst (Fig. S5, Supplementary Material). Such a highly dispersed platinum phase matching the nominal Pt weighting was also found in the highly active catalyst Pt-Co-Mo(1.0) of twice the platinum amount. However, in the catalyst with the highest Pt load Pt-Co-Mo(1.9) significant amounts of distinct Pt nanoparticles a few nm in size were observed in addition to the highly dispersed Pt phase (Figs. S5 and S6, Supplementary Material). No other elements from the element maps (e.g. sulfur) could be clearly associated with the Pt nanoparticles indicating likely metallic platinum (Fig. S6, Supplementary Material). Interestingly, a full-frame EDX quantification including both the dispersed Pt phase and Pt nanoparticles still matched the overall nominal Pt load (1.9 wt%), indicating a two-phase Pt distribution with an estimated fraction of the highly dispersed Pt phase corresponding to 1.2 wt% as measured in a selected area free of Pt nanoparticles (Fig. S5, Supplementary Material). The concentration of platinum in the highly dispersed Pt phases, as determined from the STEM-EDX analyses, thus scales with the activity gain of the catalysts at all Pt loadings (see Fig. 2a). On the other hand, the presence of Pt nanoparticles (observed occasionally in all Pt-samples samples but only to a substantial extent in the highest Pt loading samples) appear with limited or no correlation with the HDS activity. Therefore, we exclusively associate the highly dispersed platinum phase with the Pt promotional effect of the Co-Mo catalysts and attribute the activity saturation above 10000 ppm Pt in Fig. 2a to the onset of the separate Pt formation.

To shed further light on the local structure of the dispersed platinum, the activity tested Pt-Co-Mo(0.5) catalyst was *qualitatively* addressed by ex-situ X-ray absorption near edge spectroscopy (XANES). The normalized XANES spectrum recorded at the Pt L$_3$-edge (Fig. 3b) reveals edge features of the Pt-Co-Mo catalyst that in intensity and shape are close to those of PtS$_2$, indicating a similar

Christian Frederik Weise, H. Falsig, Poul Georg Moses et al.

Journal of Catalysis 403 (2021) 74–86

Fig. 3. Characterization of tested Pt-Co-Mo(0.5) catalyst. (a) HAADF-STEM image and corresponding EDX element distributions of Mo, Co and Pt. The color bars represent deconvoluted net counts for Mo-K and Co-K regions and total counts for Pt-L (noise level ~ 50% based on peak-to-background in the summed EDX spectrum). (b) Normalized X-ray absorption spectra near the L_3-edge of Pt (11.564 keV) for Pt-Co-Mo and measured references of PtS_2 and PtS. (c) and (d) High-resolution TEM images of (c) Co-Mo and (d) Pt-Co-Mo revealing MoS_2 slab structures viewed along the (0 0 1) basal plane. (e) Length and stacking height distributions of MoS_2 slab structures in Co-Mo and Pt-Co-Mo catalysts (based on 1625 and 1415 particles, respectively).

electronic configuration to platinum(IV) sulfide. Thereby the platinum in the Pt-Co-Mo catalyst is, in average, significantly different from both a metallic (Pt) state or an oxide (PtO_2) state (Supplementary Material). This also indicates limited oxidation during the sample storage prior to the measurements.

High-resolution TEM imaging was used to visualize the nano-scale structures of the tested catalysts. TEM images of the reference Co-Mo sample without Pt (rel. vol. activity = 100%) and the Pt-Co-Mo(0.5) sample (rel. vol. activity = 124%) are shown in Fig. 3c,d and reveal very similar appearance of elongated dark contrasted features with occasional two such features in pair with a separation of 0.62 nm, corresponding to the lattice distance of MoS_2 (0 0 2). Thus, the elongated dark features are attributed to MoS_2 slab structures viewed along the (0 0 1) basal plane, and as a cobalt promoted HDS catalyst the Co-Mo-S structure is assumed consistent with ref. [1,13]. The Co-Mo-S structures viewed along the (0 0 1) contour the terminating edges of the support and was not observed as free-standing, unsupported slabs. This indicates that the Co-Mo-S slabs are supported on their basal plane (0 0 1) by the alumina substrate. The length and stacking height of the Co-Mo-S slab structures were measured from the TEM images (16 different sample areas each) with very similar size distributions of predominantly single layer structures (~89%), double layers (~10%) or triple layers (<1%). The stacking degree calculated as the average number of layers in the MoS_2 (0 0 1) direction was 1.12 and 1.13 for the Pt-Co-Mo and Co-Mo catalyst, respectively, revealing only a marginal difference of < 1%. The corresponding slab lengths were found in the range from 1.2 nm to 7.5 nm with a mean size of 2.38 and 2.48 nm for the Pt-Co-Mo catalyst and Co-Mo catalyst, respectively, as determined from a lognormal fit to the entire size distribution (Fig. 3e). Thus, the Co-Mo-S and Pt-Co-Mo-S structures are similarly distributed in stacking height and slab length, and this similarity is expected to extend below the detection limit for the slab length of 1.2 nm. Based on the minute change in the average slab length the Co-Mo-S structures in the Pt-Co-Mo catalyst expose about 4% more edge sites compared to the Co-Mo sample. This minor change in edge dispersion is insufficient to fully account for the activity boost of 24% caused by addition of Pt, indicating that Pt has additional functional effects.

Recent work on enhancing the intrinsic catalytic properties of two-dimensional MoS_2 for tuning the electronic properties in improved hydrogen evolution reaction (HER) catalysts points to single atom Pt dopants of the (inert) MoS_2 basal plane [48]. The location of such Pt single atom has been reported to replace an Mo atom in the MoS_2 structure (in which Pt—S bonds are formed), or localized in S vacancies, and various unspecific positions in case of surface (carbon) contamination [49–51]. Therefore, we address possible interactions of single Pt atoms with the Co-Mo-S structure either by adsorption or substitution under HDS sulfiding conditions using density functional theory (DFT).

3.3. Single-atom Pt and specific interactions with Co-Mo-S

We have with DFT investigated the possible stable sites for Pt substitution into and adsorption on the Co-Mo-S particle. In order to do so we have chosen the 3 model structures from ref. [25] to

Christian Frederik Weise, H. Falsig, Poul Georg Moses et al.

Journal of Catalysis 403 (2021) 74–86

represent a Co-promoted MoS$_2$ particle, namely the Mo-edge, a Co-promoted S-edge and a corner site. We start out by addressing the equilibrium structures of the 3 model sites by calculating the free energy of sulfidation, $H_2S(g) + * \leftrightarrow H_2(g) + S*$, at HDS conditions (see Supplementary Material). We find at equilibrium that the Mo- and S-edge is terminated by monomeric S, whereas the corner site has a S vacancy (Fig. 4a), in accordance with [25].

We can now address the most stable sites for Pt substitution into the Co-Mo-S particle. By substitution of one Mo atom with one Pt atom in the Mo-edge model, and one Co atom with one Pt atom in the S-edge and corner models, we first obtain equilibrium structures for the Pt-Co-Mo-S sites by calculating the free energy of sulfidation and desulfidation around the Pt-promoted site at HDS conditions (Supplementary Material). The substitution free energies have then been obtained for reaction (2) and (3) and are presented in the bottom of Fig. 4a together with the Pt-Co-Mo-S edge and corner equilibrium structures. As a reference for our DFT calculations we choose PtS$_2$ (rather than PtS) since this particular platinum sulfide structure is what our XANES results indicate (Fig. 3b). We find it is energetically favorable to incorporate Pt single-atoms into both Mo- and S-edges and corner sites. The calculations indicate a slight preference of the Mo-edge over the corner site, and to a lesser extend the S-edge, however, within the uncertainty of calculations; Mo-edge: −0.50 (+/−0.44) eV, S-edge: −0.16 (+/−0.30) eV, and corner: −0.38 (+/−0.26) eV, the corner and the Mo-edge are probably equally preferred substitution sites. We have also calculated the stability of Pt and PtS adsorbed on several different adsorption sites on the Mo-edge, S-edge and the corner equilibrium structure of Co-Mo-S (see Supplementary Material). We find that Pt substitution into Co-Mo-S is significantly more stable than adsorption on the Co-Mo-S particle.

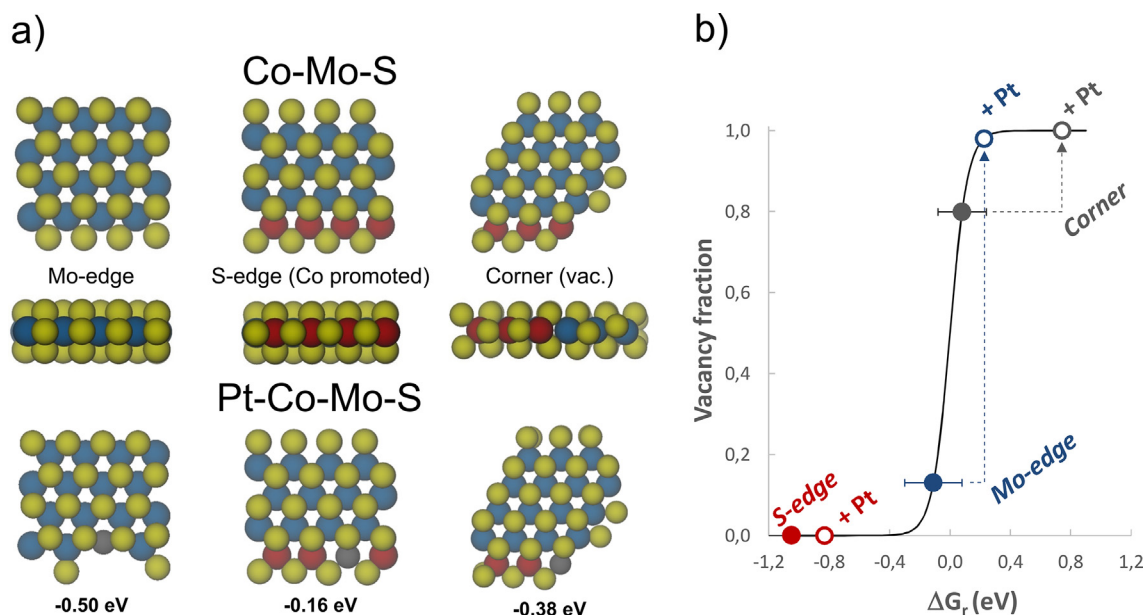Next, we address the structure of the Co-Mo-S and Pt-Co-Mo-S sites at HDS conditions (as shown in Fig. 4a) in more detail. In Fig. 4b we show how the fraction of sulfur vacancy sites on edges and corners of Co-Mo-S and Pt-Co-Mo-S structures relates to the free energy of sulfidation. We find that the free energy of sulfidation of a vacancy site at the Co-Mo-S Mo-edge is −0.11 (+/−0.19) eV, and for the corner vacancy 0.08 (+/−0.16) eV. Thus, as seen in

Fig. 4b, vacancy and monomeric S sites are likely to co-exist at the Mo-edge and corner of the Co-Mo-S particle, however, to which degree is shadowed by the uncertainty of the calculation. On the other hand, platinum single-atoms incorporated into the edges and the corner of the Co-Mo-S particle leads to a weakening of the sulfur binding energy around the Pt atom compared to the non-Pt counterpart (Fig. 4b), such that the Pt sites at the Mo-edge and corner are indeed characterized by inherently stable vacancy sites. In fact, at the Mo-edge, Pt incorporation leads to a double CUS-vacancy around the Pt atom, which is a significant restructuring compared to the non-Pt counterpart. At the S-edge we see a slight shift in the free energy of sulfidation when Pt is incorporated (Fig. 4b), however this does not lead to vacancy sites.

Double vacancy sites at the corners of Co-Mo-S have previously been suggested to be attractive for HDS [28], however, such sites are prohibited due to a high formation energy at HDS conditions. Here, we have also calculated the formation energy of such a double vacancy site from the vacancy sites at the corners of Co-Mo-S and Pt-Co-Mo-S (geometry given in Supplementary Material). At HDS conditions, we find a free energy of formation of 1.07 eV and 0.7 eV for Co-Mo-S and Pt-Co-Mo-S corners, respectively. Although Pt indeed lowers the formation energy of a double vacancy by ∼ 0.4 eV relative to the corresponding Co corner, also the Pt-corner double vacancy at these sites are unstable at HDS reaction conditions.

3.4. Identifying the active phase(s)

Visualization of the Pt-Co-Mo(0.5) catalyst at the atom-by-atom scale was approached using high-resolution STEM imaging [52–54]. Previously atomically resolved imaging of Co-Mo-S structures [13,55,56] has required use of a high-surface area carbon as carrier but we have here achieved such resolution for catalysts based on an industrially much more relevant high-surface area γ-Al$_2$O$_3$ carrier. The high-angle annular dark-field (HAADF) image contrast scales approximately as $Z^{1.7}$ where Z is the atomic number and the Pt atoms (Z = 78) therefore appear much brighter than single Mo (Z = 42) or Co atoms (Z = 27), providing the support is

a)

Co-Mo-S

Mo-edge — S-edge (Co promoted) — Corner (vac.)

Pt-Co-Mo-S

−0.50 eV — −0.16 eV — −0.38 eV

b)

Fig. 4. (a) Ball models (top and side view) showing the geometry of the Mo-edge, the S-edge and the corner site of Co-Mo-S and Pt-Co-Mo-S with the calculated main sulfur termination at HDS conditions. Mo is in blue, Co red, Pt grey and S yellow. The free energy for substitution of Pt with Mo or Co is given below each structure. (b) Vacancy fraction, $\theta_* = 1/(1 + \exp(-\Delta_r G/(k_B T)))$ versus the free energy of sulfidation, $\Delta_r G$, for $H_2S(g) + * \rightarrow S* + H_2(g)$ at HDS conditions (673 K, p(H$_2$)/p(H$_2$S) = 20). Sulfur vacancy site population at the edge and corner sites of Co-Mo-S (closed symbols) and Pt-Co-Mo-S (open symbols). Pt weakens the sulfur binding and increases the average vacancy fraction at the edge and corner sites. (For interpretation of the references to color in this figure legend, the reader is referred to the web version of this article.)

sufficiently light and thin. The industrial Co-Mo-S structures are supported on a few nm thin alumina crystallites, with dimensions and orientations occasionally thin enough for imaging single heavy metal atoms [57]. However, alumina is an insulator with a very poor electrical conductivity and charging of the sample in the electron beam complicates high-resolution imaging. Therefore, we dispersed the alumina-supported catalyst onto a TEM grid with a conducting amorphous carbon layer to compensate for the electrical resistivity of alumina at the expense of image contrast.

Fig. 5a shows a high-resolution STEM image of the Pt-Co-Mo (0.5) sample and reveals a truncated hexagonal shaped nanocrystal about 3 nm in diameter with a periodic array of bright dots indicating heavy atom columns. An intensity profile across the nanocrystal shows four intensity peaks separated by about 0.32 nm consistent with the Mo–Mo distance of MoS_2 (Fig. 5b,c). The nanocrystal is therefore attributed a MoS_2 structure viewed in (001) projection in agreement with previous studies [55]. We note that the size of the crystal is in accordance with the MoS_2 slab lengths viewed edge-on in TEM images (Fig. 3) and we show below

by comparison to STEM image simulations that the contrast is consistent with metal atoms in a single-layer slab structure.

A wider image field-of-view (Fig. S5, Supporting Material) shows the presence of both hexagonally shaped MoS_2 nanocrystals as well as more irregular shaped MoS_2 nanocrystalline domains viewed in (001) projection with multiple corner sites and kinks of a concave geometry, and even isolated (metal) single-atoms or few-atom clusters. Such a co-existence of both regular and irregular shaped MoS_2 structures in alumina-supported catalysts have previously been reported [53,54]. Furthermore, restructuring of the MoS_2 morphologies was observed in successive recorded images as an effect of the electron beam (in line with [58]) under the present imaging conditions. However, such image series also revealed distinctively bright dots associated with the edges of the MoS_2 crystals (as indicated by circles in Fig. 5b) in the first acquired images that either remained at the same position or has moved to new positions in the subsequent image (Fig. S6, Supporting Material). To address the atomic arrangement in such nanocrystals, we carry out a detailed image contrast analysis of
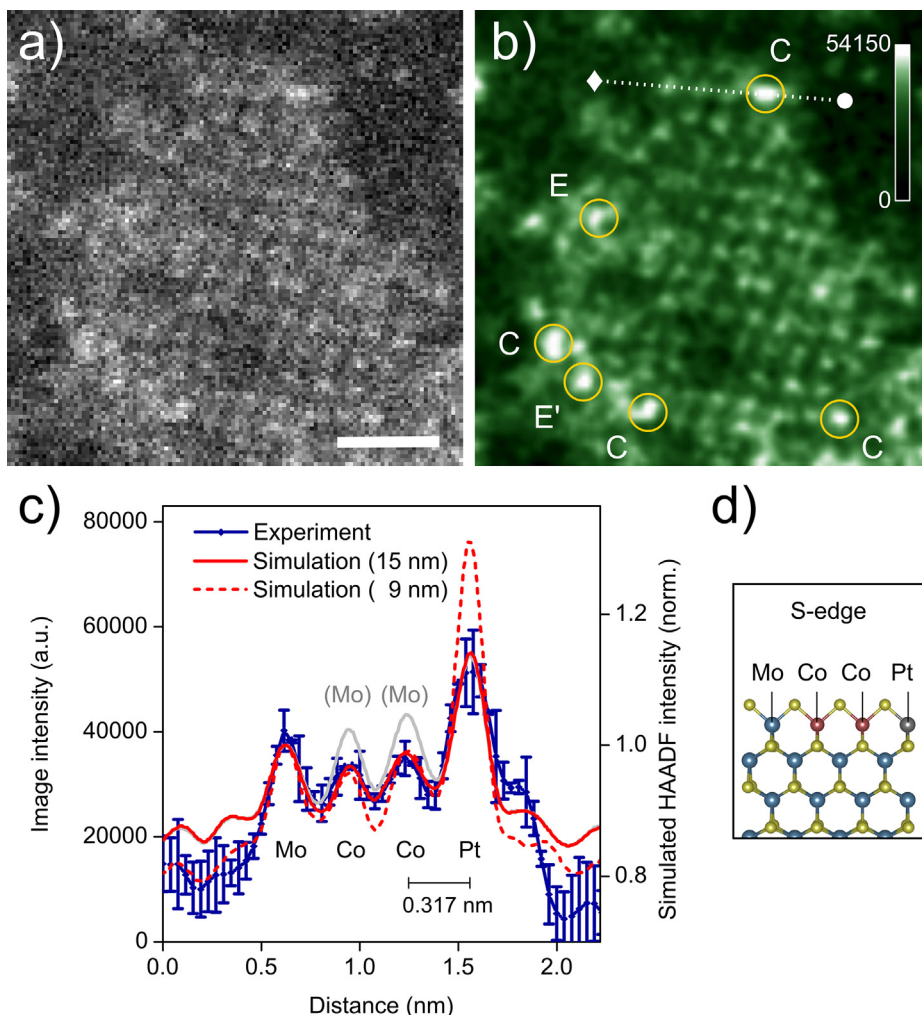
Fig. 5. High-resolution STEM imaging of the alumina supported Pt-Co-Mo(0.5) catalyst. The catalyst is imaged on top of an amorphous carbon film. (a) HAADF-STEM image (raw data) of a MoS_2 nanocrystal oriented with the [001] direction along the electron beam. Scalebar 1 nm. (b) Image in (a) shown with a Gaussian blur of radius 1 pixel, and green colored. Image intensities associated with a Pt atom (based on an intensity analysis) are marked by circles and located at corner sites (C) or edge (E) positions of the MoS_2 nanocrystal. (c) Image intensity line profile along a low-indexed edge from ◆ to ● as indicated in (b). The error bars denote the deviation of a single pixel intensity in the unprocessed image in (a) as compared to the Gaussian mean. Red curves show normalized intensity profiles from simulated HAADF-STEM images of a MoS_2 model structure (shown in (d)) supported on 9 nm and 15 nm amorphous carbon, respectively. (d) Model of the MoS_2 structure (Mo blue, S yellow) used for image simulations with 2xCo (red) and 1xPt (grey) atom substituted at metal sites at the S-edge. A reference simulation of the MoS_2 S-edge with only Mo atoms and 1xPt atom supported on 15 nm carbon is shown in grey in (c). (For interpretation of the references to color in this figure legend, the reader is referred to the web version of this article.)

the MoS_2 nanocrystal in Fig. 5, which represents a pristine area not previously exposed to the electron beam.

The intensity profile along the edge reveals three distinct contrast levels (Fig. 5c). To ease the interpretation of this contrast pattern, STEM image simulations of a supported MoS_2 structure was performed. A single-layer MoS_2 slab structure consisting of 16 metal atoms (Mo, Co, Pt) and 36 sulfur atoms was used as model for the STEM image simulations, with an edge length of 4 metal atoms (using the S-edge with 50% sulfur coverage). To overcome the effect of contrast reduction from any (alumina, carbon) support materials, the (Mo,Co,Pt)-MoS_2 model structure was placed on top of an amorphous carbon model structure with a varying thickness of 0–15 nm. Not surprisingly, in the simulated HAADF-STEM images of an unsupported or thin (3 nm) carbon supported MoS_2 the atomic (Mo) metal lattice as well as the sulfur sub-lattice could be resolved, whereas at thicker supports of 9–15 nm the sulfur columns showed significantly reduced contrast with intensities visually mixed up with the intensity fluctuations of the amorphous support (Fig. S7, Supplemental Material). This is in accordance with a thin, flat (crystalline) support like graphene or graphite being the preferred support materials for obtaining single atom sensitivity imaging of MoS_2 [55,58,59]. In contrast, however, the atomic imprints of Mo, Co or Pt single atoms were distinctly resolved in the simulated STEM images up to 15 nm of amorphous carbon support as a result of the high Z-number. In addition, image contrast of single atoms is insensitive towards small sample tilts away from a crystal zone-axis as opposed to e.g., diatomic (sulfur) columns. Thus, the following discussion will only focus on the metal atom positions.

The image contrast of the individual supported metal atoms in the simulated STEM images was quantitatively addressed by measuring the intensity maxima of the corresponding atom peak positions to evaluate the confidence level for atom identification. We find that even for the unsupported MoS_2 crystal, the peak maxima of the various Mo atoms show a range of intensities rather than a single value as a result of the comprehensive imaging model [60] used to simulate the sampling of the electron probe over the electrostatic potential of the specimen. Hence, a *distribution* of metal atom intensities measured from the HAADF-STEM images are expected. Importantly, the contrast of a single Pt atom was significantly brighter than any Mo atom or Co atom on a support thickness up to 15 nm (Fig. S9, Supplementary Information). On the other hand, the Co and Mo atoms were convincingly separated by contrast only at very thin supports (3 nm) as for thicker supports (9–15 nm) the contrast levels of Co and Mo started to overlap. The supported Co atoms, however, still appeared with lower contrast than the average Mo atom. Based on the maximum overlap of the peak intensity distributions the Co atoms could be discriminated from Mo with a confidence level of 84% on a 9–15 nm thick amorphous carbon support in the simulations.

A comparison of the experimental data and the normalized image simulations is shown in Fig. 5c. The overall contrast levels of the (experimental) MoS_2 structure and the adjacent support materials can be well described by the 9–15 nm amorphous (carbon) supported single-layer MoS_2 model structure although the (experimental) support might not be completely flat and includes alumina as well. However, the detailed contrast levels could not be fitted with single Mo and Pt atoms only (shown in grey) without exceeding the uncertainty in the image contrast given by the statistical noise in the raw image (error bars). Instead, the simulations show that two Co atoms incorporated on that edge gives a better agreement (Fig. 5c,d). That is the *relative* contrast level analysis indicates the formation of a single-layer Pt-Co-Mo nanostructure. Moreover, the tertiary Pt-Co-Mo sulfide structure provided by a Pt corner atom in the Co-Mo-S structure is an energetically stable

configuration according to our DFT results (Fig. 4). Thereby, we substantiate the argument that the nanocrystal in Fig. 5 is indeed a cobalt promoted *single layer* MoS_2 crystal (Co-Mo-S phase) with a corner Pt atom. An unambiguous atom identification may possibly only be obtained using complementary atom-scale spectroscopy with careful optimized illumination and imaging schemes [13,52]. However, with the atomic assignments in place we point to the Co promoted edge as the S-edge of the MoS_2 structure (Fig. 5d) and by symmetry, the opposite edge must be an Mo-edge.

More interestingly, from an intensity analysis of the peak maxima over the entire nanocrystal (Fig. S10, Supplementary Material), six atom positions stand out by having a significantly larger intensity more than 3x sigma above the Gaussian distribution fit to all peak maxima and includes the corner Pt atom just identified. These six atom positions are all marked by circles in Fig. 5b and are assigned Pt single atoms with four corner site positions (C) and two Pt atoms associated with the low-indexed edges (E, E'), i.e. the Mo-edge and S-edge, respectively. Based on the location of these six Pt atoms in the nanocrystal in Fig. 5 we thereby justify all the three plausible scenarios of single-atom Pt-Co-Mo-S interactions discovered by DFT calculations (Fig. 4) with indications of the corner site position being the more pronounced.

Thus, the Pt promotional effect of the industrial Co-Mo catalysts with Pt added *prior* to a sulfidation step may be associated with incorporation of Pt in the Co-Mo-S edge structures (referred to as the Pt-Co-Mo-S phase) rather than adsorption or a separate Pt (-sulfide) phase, e.g. PtS which elsewhere have been observed as a stable phase at HDS reaction condition at higher temperatures (400 °C) [61], and also suggested in the case of platinum doping of a pre-sulfided NiW catalyst [62]. The Pt-Co-Mo-S phase, however, is consistent with a Pt(IV)-sulfide resembling structure with Pt—S bonds as revealed by XANES. According to our DFT investigations, the platinum in the Pt-Co-Mo-S structure has a sulfur coordination of 3–4 under HDS conditions (Fig. 4). The linear increase in HDS activity with increased amounts of Pt (Fig. 2a) is consistent with single atoms gradually being incorporated into edge sites of a nanocrystal. In particular, the promotional effect of Pt and Co in combination at various contribution ratios (Fig. 2b) is rationalized from the incorporation of Pt in corner sites or edge sites of a partly cobalt decorated MoS_2 in which Mo and Co atoms co-exist at the S-edge as visualized by electron microscopy (Fig. 5).

In addition, the amount of Co and Pt relative to Mo per Co-Mo-S slab can be evaluated based on the nominal metal load on the catalysts using simple geometric considerations. Assuming single-layer Co-Mo-S slab structures of length ∼ 2.5 nm, this corresponds to a cluster size of N = 61 metal atom sites in a regular hexagonal shape with a side length of 4 Mo—Mo distances (5 atoms) and 9 metal atoms across the longest diameter. We find that 3.5 wt% Co corresponds to Co:Mo = 0.35 (molar ratio) which is equivalent to about 16 atoms out of the assumed average cluster size of 61 metal atoms, in case of full Co incorporation into Co-Mo-S. This would correspond to 66% of the edge metal atoms and agrees with a Co-Mo-S structure with Co decorating the S-edges only. Using a Co-Mo-S slab version with 16 Co atoms and 45 Mo atoms, the corresponding addition of Pt single atoms is Pt:Mo = 0.022, 0.044 or 0.067 (molar ratio) for 1, 2, or 3Pt atoms per Co-Mo-S slab, respectively. Hence the activity maximum at 146% of Fig. 2a occurs at a degree of Pt-promotion corresponding to Pt:Mo = 0.03–0.04 or about 2Pt atoms per Co-Mo-S slab on average. At saturation, Pt separates out into the observed competing second phase of Pt clusters at a high precursor density [50,63,64], which are probably poorly catalytically active. As minor local variations in Pt precursor or metal concentrations at the nano-scale may be expected during synthesis, it can be speculated that the origin of saturation by a few

Pt atoms per Co-Mo-S slab on average can be geometrically constrained as the corner sites of the (hexagonal) Co-Mo-S structures are gradually filled and occupied by Pt at increasing load.

3.5. Proposed HDS mechanism

With the Pt-Co-Mo-S catalyst model in mind we investigate the hydrodesulfurization of the sterically hindered 4,6-DMDBT molecules based on DFT calculations. Such 4,6-disubstituted species are present (see Supplementary Material) in the heavy end of the industrial feed used (a mix of straight run gas oil and light cycle oil) and are, due to sterically hindrance in the vicinity of the sulfur atom, the most difficult sulfur species to convert by hydrotreating. Analytics such as e.g. 2-dimensional gas chromatography show that 4,6-disubstituted DBTs constitute essentially all those organosulfur compounds that remain to be converted when a sulfur level of a few hundred ppm S has been achieved. To reach the desired ULSD target of only 10 ppm S, most of the catalyst volume in the reactor serves the purpose of desulfurizing the relatively very small amount of a few hundred ppm 4,6-disubstitued DBTs (Supplementary Material). At the test conditions employed in this study sulfur concentrations below 20 ppm were obtained in the oil exiting the reactors, i.e. concentrations well within the domain where essentially only 4,6-substituted DBTs are being converted. As the H_2 partial pressure was 30 bar, our conditions are suited for evaluating the performance of catalysts aimed at the industrial so-called low-pressure segment, i.e. Co-Mo catalysts. Industrial refiners that have decided on process equipment to produce ULSD in the high-pressure segment would use Ni-Mo rather than Co-Mo catalysts.

The exact mechanism for desulfurization of 4,6-DMDBT on Pt-Co-Mo-S is considered to be quite intricated giving the size of the molecule(s) and the complexity of the edge sites. To provide a first preliminary assessment we here address with DFT a possible

effect of Pt by investigating the stability of reaction intermediates in two hypothetical DDS and HYD reaction pathways of 4,6-DMDBT desulfurization at Pt-Co-Mo-S and Co-Mo-S sites. We especially focus on the thiolate formation, since thiolate formation has been suggested to be a starting model for which sites participate in the C—S cleavage of a sulfur containing molecule [25].

Fig. 6 shows the hypothetical DDS and HYD pathways we investigate. Species denoted with an asterisk are adsorbed species. For both the DDS and HYD pathway the first step is the adsorption of 4,6-DMDBT on the (Pt)-Co-Mo-S particle. In the DDS pathway, a thiolate intermediate (DDS-thiolate) is formed after C—S cleavage via hydrogenation. This species can then undergo a second round of C—S bond breakage to form 3,3′-DM-BP, which desorbs from the site. In the HYD pathway, the adsorbed 4,6-DMDBT is hydrogenated six times to 4,6-HH-DMDBT, such that one benzene ring has been fully hydrogenated. This species can now undergo C—S bond breakage via hydrogenation of either i) the C—S bond between the S atom and the aromatic ring or ii) the C—S bond between the S atom to the cyclohexyl ring to form a HYD-thiolate. As for the DDS pathway the thiolate undergoes a second C—S bond breakage via hydrogenation, and the desulfurized product, 3,3′-DM-CHB, leaves the site.

In Fig. 7 we show the calculated energy diagram for both the DDS and HYD pathway of 4,6-DMDBT on the Co-Mo-S and Pt-Co-Mo-S equilibrium structures of the S-egde, Mo-edge and corner sites. We have chosen also to include the Mo-edge with a single vacancy, since both the 1S terminated Mo-edge and the single vacancies are likely (see Fig. 4b).

We start out with the energetics of the DDS pathway in Fig. 7a where adsorption of 4,6-DMDBT is the first reaction step. Beginning with the Co-Mo-S structure, we find the 4,6-DMDBT molecule to adsorb strongest through physisorption at the brim site of the Mo- and S-edges, and the calculations indicate a slightly weaker physisorption to the brim of the defect (vacancy) Mo-edge site or
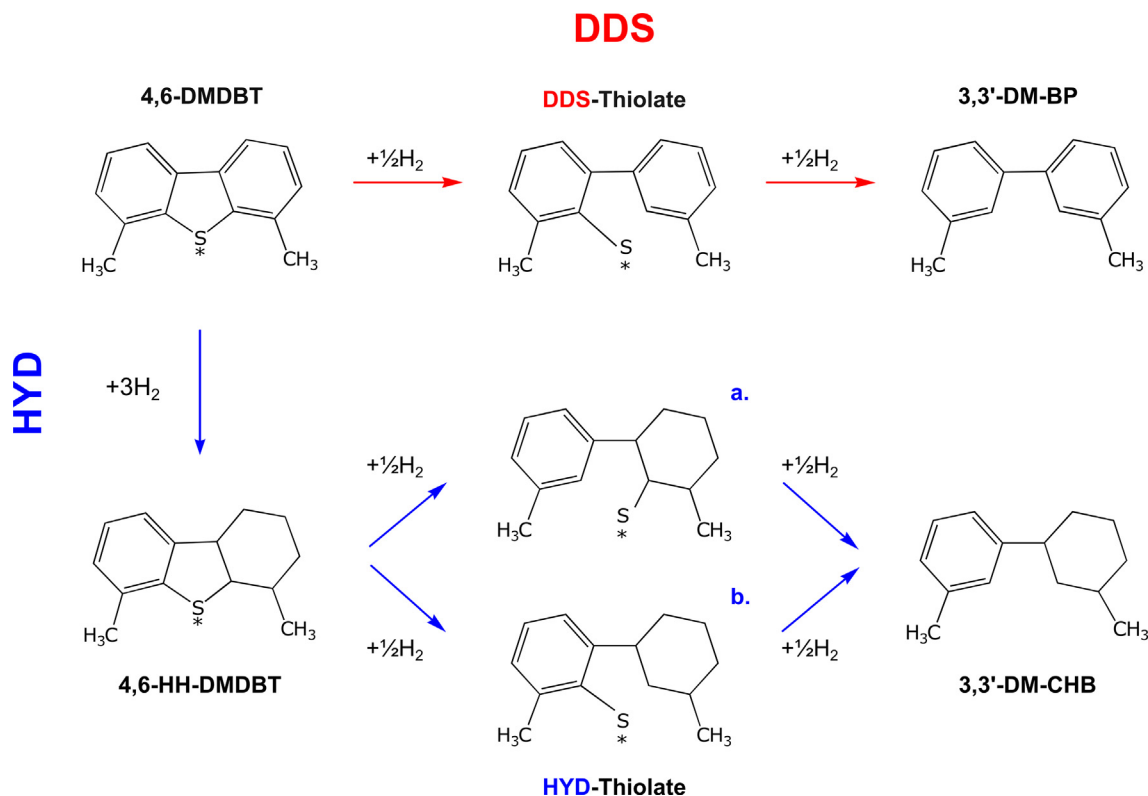

Fig. 6. Schematic showing the investigated route for the DDS (red arrow) and HYD (blue arrow) pathways for desulfurization of 4,6-DMDBT. (For interpretation of the references to color in this figure legend, the reader is referred to the web version of this article.)

Christian Frederik Weise, H. Falsig, Poul Georg Moses et al.

Journal of Catalysis 403 (2021) 74–86

corner site (see molecular configurations in Supplementary Material). At the Co-Mo-S corner, 4,6-DMDBT adsorbs equally strong physisorbed at the brim and in a chemisorbed state aligned in-plane with the particle in agreement with previous work [25] (only configurations free of the support were considered). Introducing the Pt sites in the Co-Mo-S structure slighty weakens the 4,6-DMDBT adsorption strength on both the Mo-edge and the corner site whereas essentially no effect is obtained at the S-edge.

Next we address the DDS-thiolate from 4,6-DMDBT on both Co-Mo-S and Pt-Co-Mo-S sites. According to the calculations, the DDS-thiolate is most strongly adsorbed on corner and edge

vacancy sites to which it can chemisorb, consistent with that thiolates in generel are found to adsorb strongest on defect sites [25]. However, at all investigated sites except the non-Pt promoted Co-Mo-S corner site we find, interestingly, that the DDS-thiolate formation reaction step is uphill in energy. Thus, since both the adsorption of 4,6-DMDBT and the thiolate formation reaction step is energetically preferred on Co-Mo-S (corner sites) over Pt-Co-Mo-S, these calculations suggest that Pt sites has limited or no promotional effect for the DDS pathway.

We now turn to the HYD pathway for which the energetics is shown in Fig. 7b. Here the adsorbed 4,6-DMDBT is hydrogenated
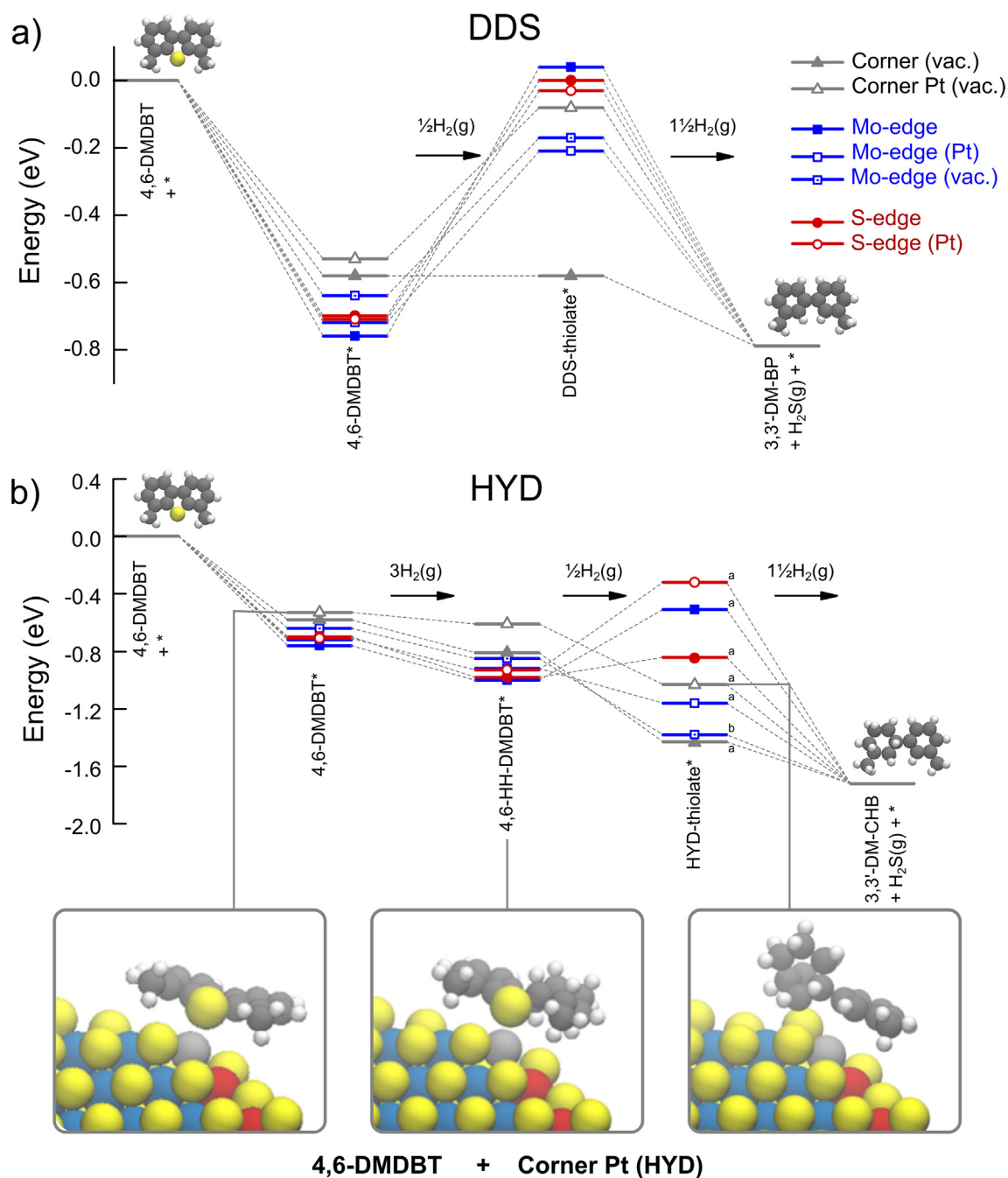
Fig. 7. Calculated energy diagram for both a) DDS and b) HYD pathway of 4,6-DMDBT on the Co-Mo-S and Pt-Co-Mo-S equilibrium structures of the S-egde, Mo-edge and corner sites. The energy level presented for the HYD-thiolate is for the most stable of thiolate *a* and *b* (see Fig. 6). The ball models show an example of an energetically favorable hydrogenation route via a corner Pt site. The energy of $H_2(g)$ and $H_2S(g)$ are described by their free energies at HDS relevant pressures and temperature, whereas 4,6-DMDBT, the adsorbed species and the desulfurized products are described by the electronic energy at 0 K. This choice is based on the unknown state of 4,6-DMDBT being a liquid or gas at HDS conditions and which thermal correction to apply to the electronic energy of the reactant is therefore unclear. For consistency, the adsorbed reaction intermediates and products are also, as the reactant, described by the electronic energy.

Christian Frederik Weise, H. Falsig, Poul Georg Moses et al.

Journal of Catalysis 403 (2021) 74–86

to 4,6-HH-DMDBT before the C—S bond is cleaved and the corresponding thiolate is formed. For the Co-Mo-S and Pt-Co-Mo-S structure, as for 4,6-DMDBT we find that 4,6-HH-DMDBT preferentially physisorbs at the brim of the 1S-terminated Mo- and S-edges and with a weaker chemisorption in-plane with the particle for the corner sites (see Supplementary Material for molecular structures). The HYD-thiolate, resulting from 4,6-HH-DMDBT, adsorbs preferentially to the vacancy sites through chemisorption by the S-part of the molecule to the vacancy. This is valid for both the HYD-thiolate *a* and *b* (see Supplementary Material). However, on all sites, except on the vacancy site of the Mo-edge, the HYD-thiolate *a,* formed from breaking the C—S bond between the aromatic ring and the S-atom, is more stable than HYD-thiolate *b* resulting from breaking the C—S bond between the S-atom and the cyclohexyl ring. Importantly, we find the formation of the HYD-thiolate to be energetically favourable on vacancy sites and unfavourable on 1S-terminated sites, suggesting that vacancy sites could be key sites for the final steps of desulfurization of 4,6-DMDBT. Here, we have not considered energy barriers for thiolate formation, however, it has been found that barriers for thiolate formation specifically from thiophene and dibenzothiophene are significantly lower on defect sites at the Mo-edge and the corner, than on the 1S-terminated S-edge [25]. We also note that the HYD-thiolate formation is significantly more favourable on all vacancy sites of both the Co-Mo-S and Pt-Co-Mo-S structure than the strongest DDS-thiolate formation on the Co-Mo-S corner, indicating desulfurization of 4,6-DMDBT proceeds primarily via the HYD pathway, consistent with experimental findings on a Co-Mo catalyst [21,22]. Overall, this could suggest that different sites may participate in the desulfurization such that 4,6-DMDBT preferentially is hydrogenated at the 1S-terminated brim of the particle, where we find the strongest adsorption of 4,6-DMDBT and the hydrogenated intermediate, and the hydrogenated species then diffuse to a vacancy site, where the final desulfurization of 4,6-DMDBT takes place.

The reactivity of corner sites of Co-Mo-S has recently attracted attention [25,65] and specifically adsorption of 4,6-DMDBT molecules has been observed by STM to occur particularly at corner (vacancy) sites [28]. Thus, a corner platinum site in the Co-Mo-S structure, as visualized in the present study, is obviously highly intriguing. Even though intermediates in the HYD pathway adsorb weaker to the Pt-corner in Pt-Co-Mo-S than the corresponding Co-Mo-S corner, the inherent vacancy site of the Pt-Co-Mo-S corner still favors HYD-thiolate formation (Fig. 7b and Supplementary Material). Likewise, at the Mo-edge the single-atom Pt incorporation promotes a double CUS site for which the calculations indicate HYD-thiolate formation is favored. Double CUS sites at the Mo-edge generated in the presence of thiophene was recently observed by STM [66] and suggested to activate the (Mo)-edges of MoS$_2$ towards sterically hindered molecules. Thus, the Mo-edge of the Pt-Co-Mo-S structure provides such double CUS sites available intrinsically, which may also explain enhanced HDS activities [38] of Pt-MoS$_2$ systems without cobalt. Therefore, we propose that the high reactivity of Pt-Co-Mo catalysts is obtained by lowering the sulfur binding energy around the Pt single-atoms at corners and (Mo)-edges in a Pt-Co-Mo-S phase making such vacancy sites more abundant (Fig. 4b). The Pt sites in the catalyst still has ability to bind 4,6-DMDBT and especially the HYD-thiolate sufficiently to favor its formation. This could suggest that despite a weaker S-binding, these sites maintain reactivity towards C—S scission of hydrogenated reaction intermediates from 4,6-DMDBT, although more elaborate studies are needed to address that in detail.

Finally, the presence of highly irregular shaped MoS$_2$ crystal morphologies observed in the tested HDS catalysts indicates the availability of other site geometries than the low-index edge struc-

tures and corner sites considered in the DFT models in the present analysis, e.g., kink sites of a concave geometry, which can be speculated to mediate hydrogenation and desulfurization favorable sites in combination. Thus, the concentration of catalytically important edges under industrial operations, i.e. the evolution in the number of a particular atomic site geometry, are key to HDS catalysis which in turn depends on the activation procedure of the catalyst (e.g. gas phase sulfidation vs. liquid sulfidation [67,68]), operating conditions, and promoters as well.

4. Conclusion

The present work demonstrates a tertiary transition metal sulfide-based catalyst for hydrotreating processes. Addition of ppm-levels of Pt to an industrial Co-Mo-S catalyst leads to a remarkable increase of up to 46%, as compared to the Pt-unpromoted catalyst, in the activity for low-pressure hydrotreating aimed at producing ultra-low sulfur diesel oil. This boosted performance is attributed to the Pt atoms incorporated into terminating edge and corner sites of the Co-Mo-S nanostructure as resolved by combining X-ray absorption spectroscopy and atomic-resolution electron microscopy. Interplay with density functional theory calculations suggests that Pt acts by reducing the sulfur binding energy under HDS conditions compared to the Co-Mo-S structure only. This mechanistic effect is most pronounced at the Pt-promoted corner site and at the Mo-edge. Since the Pt favors CUS formation and the simple probe HYD-thiolate adsorption is similar on the Pt promoted and unpromoted vacancy sites, the role of Pt is speculated to create sites for favorable adsorption of sterically hindered molecules such as 4,6-DMDBT to undergo desulfurization utilizing a functionality of adjacent Mo- and S-edges, or corner sites synergistically.

Declaration of Competing Interest

The authors declare that they have no known competing financial interests or personal relationships that could have appeared to influence the work reported in this paper.

Acknowledgement

Appendix A. Supplementary material

Supplementary data to this article can be found online at https://doi.org/10.1016/j.jcat.2021.03.008.

References

[1] J.R. Anderson, M. Boudart (Eds.), Hydrotreating Catalysis, Science and Technology, vol. 11, Springer, Berlin, 1996.
[2] R. Prins, V.H.J. de Beer, G.A. Somorjai, Catal. Rev.-Sci. Eng. 31 (1–2) (1989) 1–41.
[3] T. Kabe, A. Ishihara, W. Qian, Hydrodesulfurization and hydrodenitrogenation, Chem. Eng. 1 (1999).
[4] C. Song, Catal. Today 86 (1) (2003) 211–263.
[5] C. Song, In memoriam of Dr. Henrik Topsøe (1944–2019), Advances in Catalysis 65 (2019), Pages xiii-xx.
[6] A.C. Byrns, W.E. Bradley, M.W. Lee, Ind. Eng. Chem. 35 (11) (1943) 1160–1167.

[7] B.S. Clausen, S. Mørup, H. Topsøe, R. Candia, J. Physique Colloq. 37 (1976) C6–249.
[8] R. Candia, B.S. Clausen, S. Mørup, H. Topsøe, J. Catal. 68 (2) (1981) 453–463.
[9] C. Wivel, B.S. Clausen, R. Candia, S. Mørup, H. Topsøe, J. Catal. 87 (1984) 497–513.
[10] H. Topsøe, R. Candia, N.-Y. Topsøe, B.S. Clausen, Bull. Soc. Chim. Belg. 93 (1984) 783–806.
[11] B.S. Clausen, H. Topsøe, R. Candia, J. Villadsen, B. Lengeler, J. Als-Nielsen, F. Christensen, J. Phys. Chem. 85 (25) (1981) 3868–3872.
[12] J.V. Lauritsen, S. Helveg, E. Lægsgaard, I. Stensgaard, B.S. Clausen, H. Topsøe, F. Besenbacher, J. Catal. 197 (1) (2001) 1–5.
[13] Y. Zhu, Q.M. Ramasse, M. Brorson, P.G. Moses, L.P. Hansen, C.F. Kisielowski, S. Helveg, Angew. Chem. Int. Ed. 53 (40) (2014) 10723–10727.
[14] P. Raybaud, J. Hafner, G. Kresse, S. Kasztelan, H. Toulhoat, J. Catal. 190 (1) (2000) 128–143.
[15] H. Schweiger, P. Raybaud, G. Kresse, H. Toulhoat, J. Catal. 207 (1) (2002) 76–87.
[16] M.V. Bollinger, J.V. Lauritsen, K.W. Jacobsen, J.K. Nørskov, S. Helveg, F. Besenbacher, Phys. Rev. Lett. 87 (19) (2001) 196803.
[17] P.G. Moses, B. Hinnemann, H. Topsøe, J.K. Nørskov, J. Catal. 248 (2) (2007) 188–203.
[18] S. Rangarajan, M. Mavrikakis, ACS Catal. 7 (1) (2017) 501–509.
[19] B.C. Gates, H. Topsøe, Polyhedron 16 (18) (1997) 3213–3217.
[20] X. Li, A. Wang, M. Egorova, R. Prins, J. Catal. 250 (2) (2007) 283–293.
[21] M. Egorova, R. Prins, J. Catal. 241 (1) (2006) 162–172.
[22] F. Bataille, J.-L. Lemberton, P. Michaud, G. Pérot, M. Vrinat, M. Lemaire, E. Schulz, M. Breysse, S. Kasztelan, J. Catal. 191 (2) (2000) 409–422.
[23] F. Besenbacher, M. Brorson, B.S. Clausen, S. Helveg, B. Hinnemann, J. Kibsgaard, J.V. Lauritsen, P.G. Moses, J.K. Nørskov, H. Topsøe, Catal. Today 130 (1) (2008) 86–96.
[24] P.G. Moses, B. Hinnemann, H. Topsøe, J.K. Nørskov, J. Catal. 268 (2) (2009) 201–208.
[25] M. Šarić, J. Rossmeisl, P.G. Moses, J. Catal. 358 (2018) 131–140.
[26] J.V. Lauritsen, M. Nyberg, J.K. Nørskov, B.S. Clausen, H. Topsøe, E. Lægsgaard, F. Besenbacher, J. Catal. 224 (1) (2004) 94–106.
[27] A.K. Tuxen, H.G. Füchtbauer, B. Temel, B. Hinnemann, H. Topsøe, K.G. Knudsen, F. Besenbacher, J.V. Lauritsen, J. Catal. 295 (2012) 146–154.
[28] S.S. Grønborg, M. Šarić, P.G. Moses, J. Rossmeisl, J.V. Lauritsen, J. Catal. 344 (2016) 121–128.
[29] J. Kibsgaard, A. Tuxen, K.G. Knudsen, M. Brorson, H. Topsøe, E. Lægsgaard, J.V. Lauritsen, F. Besenbacher, J. Catal. 272 (2) (2010) 195–203.
[30] L.S. Byskov, J.K. Nørskov, B.S. Clausen, H. Topsøe, J. Catal. 187 (1) (1999) 109–122.
[31] Z. Cinibulk, Z. Vít, Appl. Catal. A: Gen. 204 (1) (2000) 107–116.
[32] Z. Vít, J. Cinibulk, React. Kinet. Catal. Lett. 72 (2) (2001) 189–194.
[33] Z. Vít, J. Cinibulk, React. Kinet. Catal. Lett. 77 (1) (2002) 43–49.
[34] J. Cinibulk, Z. Vít, Stud. Surf. Sci. Catal. 143 (2002) 443–451.
[35] J. Cinibulk, D. Gulková, Y. Yoshimura, Z. Vít, Appl. Catal. A: Gen. 255 (2) (2003) 321–329.
[36] Z. Vít, Appl. Catal. A: Gen. 322 (2007) 142–151.
[37] Z. Vít, J. Cinibulk, D. Gulková, Appl. Catal. A: Gen. 272 (1–2) (2004) 99–107.
[38] Z. Vít, D. Gulková, L. Kaluza, M. Zdrazil, J. Catal. 232 (2) (2005) 447–455.
[39] D. Gulková, Y. Yoshimura, Z. Vít, Appl. Catal. B: Environ. 87 (3–4) (2009) 171–180.
[40] K. Herbst, M. Brorson, A. Carlsson, J. Mol. Catal. A: Chemical 325 (1–2) (2010) 1–7.
[41] H. Liu, C. Yin, H. Li, B. Liu, X. Li, Y. Chai, Y. Li, C. Liu, Fuel 129 (2014) 138–146.
[42] G.H. Singhal, W.E. Winter Jr, K.L. Riley, K.L. Trachte, U.S. Patent No. 5,152,885. Washington, DC: U.S. Patent and Trademark Office, 1992
[43] J.J. Mortensen, L.B. Hansen, K.W. Jacobsen, Phys. Rev. B 71 (3) (2005) 035109.
[44] J. Enkovaara, C. Rostgaard, J.J. Mortensen, J. Chen, M. Du Lak, L. Ferrighi, J. Gavnholt, C. Glinsvad, V. Haikola, H.A. Hansen, H.H. Kristoffersen, M. Kuisma, A.H. Larsen, L. Lehtovaara, M. Ljungberg, O. Lopez-Acevedo, P.G. Moses, J. Ojanen, T. Olsen, V. Petzold, N.A. Romero, J. Stausholm-Møller, M. Strange, G.A. Tritsaris, M. Vanin, M. Walter, B. Hammer, H. Häkkinen, G.K.H. Madsen, R.M. Nieminen, J.K. Nørskov, M. Puska, T.T. Rantala, J. Schiøtz, K.S. Thygesen, K.W. Jacobsen, J. Phys. Cond. Mat. 22 (25) (2010) 253202.
[45] J. Wellendorff, K.T. Lundgaard, A. Møgelhøj, V. Petzold, D.D. Landis, J.K. Nørskov, T. Bligaard, K.W. Jacobsen, Phys. Rev. B 85 (23) (2012) 235149.
[46] S.R. Bahn, K.W. Jacobsen, Comput. Sci. Eng. 4 (3) (2002) 56–66.
[47] C.J. Cramer, Essentials in Computational Chemistry: Theories and Models, second ed., Wiley, 2004.
[48] J. Mao, Y. Wang, Z. Zheng, D. Deng, Front. Phys. 13 (4) (2018) 138118.
[49] J. Deng, H. Li, J. Xiao, Y. Tu, D. Deng, H. Yang, H. Tian, J. Li, P. Rena, X. Bao, Energy Environ. Sci. 8 (2015) 1594–1601.
[50] H. Li, S. Wang, H. Sawada, G.G. Han, T. Samuels, C.S. Allen, A.I. Kirkland, J.C. Grossman, J.H. Warner, ACS Nano 11 (3) (2017) 3392–3403.
[51] X. Li, J.K. Lee, Y. Lu, M.A. Gerkman, E.S. Kengmana, M.V. Fonseca, J.H. Warner, G.G.D. Han, Chem. Mater. 32 (6) (2020) 2541–2551.
[52] O.L. Krivanek, M.F. Chisholm, V. Nicolosi, T.J. Pennycook, G.J. Corbin, N. Dellby, M.F. Murfitt, C.S. Own, Z.S. Szilagyi, M.P. Oxley, S.T. Pantelides, S.J. Pennycook, Nature 464 (7288) (2010) 571–574.
[53] B. Baubet, M. Girleanu, A.S. Gay, A.L. Taleb, M. Moreaud, F. Wahl, V. Delattre, E. Devers, A. Hugon, O. Ersen, P. Afanasiev, P. Raybaud, ACS Catal. 6 (2) (2016) 1081–1092.
[54] L. Zavala-Sanchez, X. Portier, F. Maugé, L. Oliviero, Nanotechnology 31 (3) (2019) 035706.
[55] L.P. Hansen, Q.M. Ramasse, C. Kisielowski, M. Brorson, E. Johnson, H. Topsøe, S. Helveg, Angew. Chem. Int. Ed. 50 (43) (2011) 10153–10156.
[56] C. Kisielowski, Q.M. Ramasse, L.P. Hansen, M. Brorson, A. Carlsson, A.M. Molenbroek, H. Topsøe, S. Helveg, Angew. Chem. Int. Ed 49 (15) (2010) 2708–2710.
[57] P.D. Nellist, J.S. Pennycook, Science 274 (5286) (1996) 413–415.
[58] B.C. Bayer, R. Kaindl, M.R.A. Monazam, T. Susi, J. Kotakoski, T. Gupta, D. Eder, W. Waldhauser, J.C. Meyer, ACS Nano 12 (8) (2018) 8758–8769.
[59] R. Zan, Q.M. Ramasse, R. Jalil, T. Georgiou, U. Bangert, K.S. Novoselov, ACS Nano 7 (11) (2013) 10167–10174.
[60] C.T. Koch, Determination of Core Structure Periodicity and Point Defect Density Along Dislocations, PhD Thesis, 2002, Arizona State University.
[61] T.A. Pecoraro, R.R. Chianelli, J. Catal. 67 (2) (1981) 430–445.
[62] S. Pessayre, C. Geantet, R. Bacaud, M. Vrinat, T.S. N'Guyen, Y. Soldo, J.L. Hazemann, M. Breysse, Ind. Eng. Chem. Res. 46 (12) (2007) 3877–3883.
[63] S. Wang, H. Sawada, X. Han, S. Zhou, S. Li, Z.X. Guo, A.I. Kirkland, J.H. Warner, ACS Nano 12 (6) (2018) 5626–5636.
[64] J. Lee, E.J. Jang, D.G. Oh, J. Szanyi, J.H. Kwak, J. Catal. 385 (2020) 204–212.
[65] S. Li, Y. Liu, X. Feng, X. Chen, C. Yang, Mol. Catal. 463 (2019) 45–53.
[66] N. Salazar, S. Rangarajan, J. Rodríguez-Fernández, M. Mavrikakis, J.V. Lauritsen, Nature Comm. 11 (1) (2020) 1–9.
[67] L.P. Hansen, E. Johnson, M. Brorson, S. Helveg, J. Phys. Chem. C 118 (39) (2014) 22768–22773.
[68] L. van Haandel, A. Longo, W. Bras, E.J. Hensen, T. Weber, ChemCatChem 11 (20) (2019) 5013–5017.